include the effects described here that are attributable to the large-scale surface topography. Quantitative analysis of the Clementine thermal infrared imaging experiment can begin once the instrument calibration to radiance is completed. Incorporation of Apollo 17 infrared observations (*18*) will allow interpretation of surface physical properties at selected locations.

An important objective of the Clementine program was to investigate the effects of the space radiation environment on the advanced technologies and lightweight spacecraft components being flight-tested on board the Clementine spacecraft and the Interstage Adapter satellite. A charged particle telescope (CPT) was built, tested, and integrated on board the main Clementine spacecraft to measure the fluxes of energetic electrons and protons encountered by the spacecraft throughout its mission. The low-energy electron channels (25 to 500 keV) have provided extensive data on the interaction between the moon and the Earth's magnetotail: While orbiting the moon, the CPT saw the wake created by the moon when it blocked the flow of energetic particles along magnetotail field lines. The CPT has also observed numerous bursts of energetic electrons during geomagnetic storms and magnetospheric substorms. A particularly important goal of the CPT was to measure fluxes of energetic protons in the energy range 3 to 80 MeV, which are emitted during solar energetic particle events. A strong solar particle event was observed on 20 to 25 February 1994 and was associated with a very strong interplanetary shock wave passage at ~0900 UT on 21 February. The Clementine CPT observed this particle event and detected the precise time and position of the shock passage. The Clementine data were particularly valuable because they were obtained concurrently with measurements from several other near-Earth spacecraft (GOES-7, SAMPEX, GEOTAIL), thus permitting a remarkable multipoint study of the shock interaction with geospace (Fig. 8).

REFERENCES AND NOTES

1. A computer with a capacity of 1.7 million instructions per second (MIPS) used for safemode, attitude control, and housekeeping. A reduced-instruction set computer (RISC) 32-bit processor operating at 18 MIPS was used for image processing and autonomous operations. Also incorporated is a state-of-the-art image compression system provided by the French Space Agency (CNES). A data handling unit with its own microcontroller sequenced the cameras, operated the image compression system, and directed the data flow. During imaging operations, the data were stored in a 3-kg, 2-gigabit dynamic solid-state data recorder and later transferred to the ground stations using a downlink operating at 128 kilobits (kb) per second. The spacecraft was commanded by a 1-kb/s uplink from the NASA Deep Space Network and Department of Defense stations. Demonstration of autonomous navigation, including autonomous orbit determination, was a major goal of the Clementine mission. Autonomous operations were conducted in lunar orbit. Data compression was done on board by the CNES compression chip. This processing was performed on a completed, framed image before storage on the solid-state data recorder when the appropriate compression flag was set. The compression chip, developed by Matra Marconi (location) under CNES specifications, could be used in two modes, selectable by an uplink command. The first optimized root-mean-square error (for a nominal compression). The second mode (JPEG) provided visual optimization at a fixed compression rate. In the first mode, blocks of 8 by 8 pixel 8-bit data are transformed to a best-fit cosine series expansion in the orthogonal row and column directions. This algorithm tends to preserve high-frequency information with less loss than does JPEG at the same compression ratio. The nominal amount of compression was set by limiting the scene error induced by compression to a fraction of the camera's temporal noises. Analysis of lunar images during the first part of the mission showed that the quantitization matrix used by the chip was optimum for the imaging cameras. The HIRES camera was operated in JPEG mode. The high-frequency information in the HIRES scenes was spurious (it was caused by nonuniformity of the gain of the intensifier tube); eliminating high-frequency content allowed higher compression without harming the information content of the scenes. The average compression rate for all images obtained during the mission was 5.5.
2. P. G. Lucey *et al.*, *Science* **266**, 1855 (1994).
3. A. S. McEwen *et al.*, *ibid.*, p. 1858.
4. C. M. Pieters *et al.*, *ibid.*, p. 1844.
5. E. M. Shoemaker *et al.*, *ibid.*, p. 1851.
6. K. Watson, B. C. Murray, H. Brown, *J. Geophys. Res.* **66**, 3033 (1961); J. R. Arnold, *ibid.* **84**, 5659 (1979); A. P. Ingersoll, T. Svitek, B. C. Murray, *Icarus* **100**, 40 (1992).
7. P. D. Spudis *et al.*, *Science* **266**, 1848 (1994).
8. M. T. Zuber *et al.*, *ibid.*, p. 1839.
9. B. W. Hapke, *Icarus* **67**, 246 (1986).
10. ———, *ibid.* **88**, 407 (1990).
11. ———, R. M. Nelson, W. D. Smythe, *Science* **260**, 509 (1993).
12. D. L. Domingue, B. W. Hapke, G. W. Lockwood, D. T. Thompson, *Icarus* **90**, 30 (1991).
13. Precision is about 1 K at a surface brightness temperature of 400 K, 2 K at 300 K, and 10 K at 210 K. The DN correspondence is 100 DN to about 400 K, 25 DN to 300 K, and 2 DN to 200 K.
14. D. F. Winter, *Radio Sci.* **2**, 229 (1970); J. M. Saari and R. W. Shorthill, *Moon* **5**, 161 (1972); R. W. Shorthill, in *Thermal Characteristics of the Moon,* J. W. Lucas, Ed. (MIT Press, Cambridge, MA, 1972), pp. 3–50.
15. A. E. Wechsler, P. E. Glaser, J. A. Fountain, in *Thermal Characteristics of the Moon,* J. W. Lucas, Ed. (MIT Press, Cambridge, MA, 1972), pp. 215–242; B. M. Jakosky, in preparation.
16. P. G. Lucey, *Proc. Lunar Planet. Sci. Conf.* **21**, 417 (1991); D. B. Nash *et al.*, *J. Geophys. Res.* **98**, 23535 (1993).
17. P. E. Johnson, K. J. Vogler, J. P. Gardner, *J. Geophys. Res.* **98**, 20825 (1993); K. V. Vogler, P. E. Johnson, R. W. Shorthill, *Icarus* **92**, 80 (1991).
18. W. W. Mendell and F. J. Low, *Moon* **9**, 97 (1974).
19. The LWIR images had a space background subtracted and had hot pixels removed by means of a median filter. A flat field shows variations in pixel sensitivity that are much smaller than the observed geographic variation; the flat-field variation has not been corrected.

16 September 1994; accepted 15 November 1994

The Shape and Internal Structure of the Moon from the Clementine Mission

Maria T. Zuber,* David E. Smith, Frank G. Lemoine, Gregory A. Neumann

Global topographic and gravitational field models derived from data collected by the Clementine spacecraft reveal a new picture of the shape and internal structure of the moon. The moon exhibits a 16-kilometer range of elevation, with the greatest topographic excursions occurring on the far side. Lunar highlands are in a state of near-isostatic compensation, whereas impact basins display a wide range of compensation states that do not correlate simply with basin size or age. A global crustal thickness map reveals crustal thinning under all resolvable lunar basins. The results indicate that the structure and thermal history of the moon are more complex than was previously believed.

Though formed in the same part of the solar system, the Earth and moon have followed dramatically different evolutionary paths in their 4.6-billion-year histories. Absolute ages of the lunar surface revealed by the Apollo missions (*1*) demonstrate that volcanism and tectonism indicative of substantial heat loss from the lunar interior essentially ceased by 2.5 to 3 billion years ago, in contrast to Earth, which remains geologically active to the present day. The fundamental difference in thermal evolution between the Earth and moon has typically been attributed to the planets' different size and mass (*2*)—the moon contained fewer radiogenic heat-producing elements because of its smaller volume and cooled faster because of its higher surface area-to-volume ratio as compared with Earth. Beyond this basic knowledge, however, understanding of the thermomechanical evolution of the moon has been elusive, largely because of limited knowledge of lunar internal structure.

The Clementine mission, sponsored by the Ballistic Missile Defense Organization, with participation from NASA, mapped the moon from late February through early May 1994 (*3*). Included in the spacecraft instrument complement were a laser ranging device and an S-band microwave transponder from which topographic and gravitational information, respectively, were collected for most of the moon. These data hold the promise of greatly improving our understanding of the lunar interior. In this report, we describe the derivation of topographic and gravitational field models from the Clementine data and use this information to characterize the shape of the moon, define the power spectral properties of the global fields, and map the distribution of crustal thickness. We also address preliminary implications of the data for the understanding of lunar structure and evolution.

The Clementine spacecraft carried a laser ranging instrument (LIDAR) that measured the slant range from the spacecraft to the lunar surface at spacecraft altitudes of 640 km or less (*3*). The instrument collected data for approximately one-half hour per 5-hour orbit during the 2-month lunar mapping mission. For the first month, with spacecraft periapsis at latitude −30°, topographic profiles were obtained in the approximate latitude range −75° to +15°, whereas in the second month of mapping, with spacecraft periapsis at latitude +30°, profiles were obtained in the approximate range −15° to +75°.

To produce a global topographic data set from the lidar system, we first subtracted a precise orbit from the range profiles. We computed these orbits with the GEODYN/SOLVE orbital analysis programs (*4*). We converted the timing of the arrival of the laser pulse on the lunar surface to selenocentric coordinates by interpolating the spacecraft orbital trajectory to the time of the laser pulse, which accounted for the one-way light time to the surface. The observed range from the spacecraft to the surface was transformed to a radius measurement in a lunar center-of-mass reference frame. Our orbits were characterized by a formal uncertainty in radial position of about 10 m and have an accuracy with respect to the lunar center of mass of better than 100 m, which is comparable to the single-shot ranging precision of the lidar (40 m). The radial orbit accuracy thus determines to first order the accuracy of the global topographic model. In the topographic data set presented here, we did not include a correction for spacecraft pointing errors, which were at the milliradian level (*5*) and are insignificant compared with the instrument ranging precision and orbit error.

The LIDAR typically ranged once per 0.6 s, expending over half a million laser shots during the 2-month Clementine lunar mapping mission. The instrument detector triggered on 19% of the shots. To distinguish valid ranges from noise hits for these ~114,000 triggers (*6*), we applied a Kalman filter based on a stochastic model of topographic variance (*7*). We developed the filter on the basis of the known power-spectral distribution of the topography of the moon (*8*), which made it possible to predict the likely dynamic range of topographic power over a specified spatial distance such as the along-track or cross-track laser shot spacing. Filtering the data yielded ~72,300 "valid" ranges.

These data were assembled into a 2° by 2° grid in the latitude range from −75° to +75°. Figure 1 is a location map that shows that most major lunar basins were sampled by Clementine altimetry. The elevations were referenced to a spheroid with a radius of 1738 km and flattening of 1/3234.93, the latter corresponding to the C_{20} spherical harmonic term we obtained for the lunar gravity field (see below). This is the observed dynamical flattening of the planet and is greater than the flattening for a hydrostatic ellipsoid. We did a 70th-degree and -order spherical harmonic expansion (half-wavelength resolution ~80 km) of the data set to yield the topographic model designated Goddard Lunar Topography Model 1 (GLTM-1) (Fig. 2A). In this and other maps, the lunar near side (the side visible from Earth) is on the right side of the figure, and the lunar far side is on the left.

This topographic model represents the first reliable global characterization of surface heights for the moon. The moon exhibits a dynamic range of topography of about 16 km, which is over 30% greater than the range noted in previous reports based on Apollo laser measurements and Earth-based radar and limb measurements (*8, 9*). This difference is due to better coverage: The greatest variations in lunar topography are on the far side over a broad band of latitude. Previous topographic measurements of the moon's far side were limited to equatorial swaths covered by the Apollo laser altimeters (*9*). Where Apollo and Clementine coverage overlap, measured relative topographic heights generally agree to within ~500 m, with the difference due to our more accurate orbit corrections and to noncoincidence of laser measurements. As was previously noted by the Apollo altimetry (*9*), Clementine topography shows the lava-flooded mare basins to be extremely level, with typical slopes of less than one part in 10^3.

The most pronounced topographic feature on the moon is the South Pole–Aitken Basin (180°E, 56°S). With a diameter of 2500 km and a maximum depth of 8.2 km below the reference ellipsoid, this structure was first identified in lunar images (*10, 11*). From Clementine altimetry, we recognize this structure to be the largest and deepest impact basin in the solar system. Maria Humboltianum, Crisium, and Fecunditatis, all in the longitude range 40°E to 80°E, also constitute distinctive topographic lows. The highest topography of 8 km above the reference ellipsoid occurs on the lunar far side in the highlands north of the Korolev Basin (205°E, 5°N), adjacent to the South Pole–Aitken structure that represents the lowest elevation on the moon.

Some structures that were suspected ancient impact basins display distinct topographic depressions. A notable feature is the Mendel-Rydberg Basin (275°E, 52°S), just south of Mare Orientale, which had been proposed as an impact basin (*11*), but

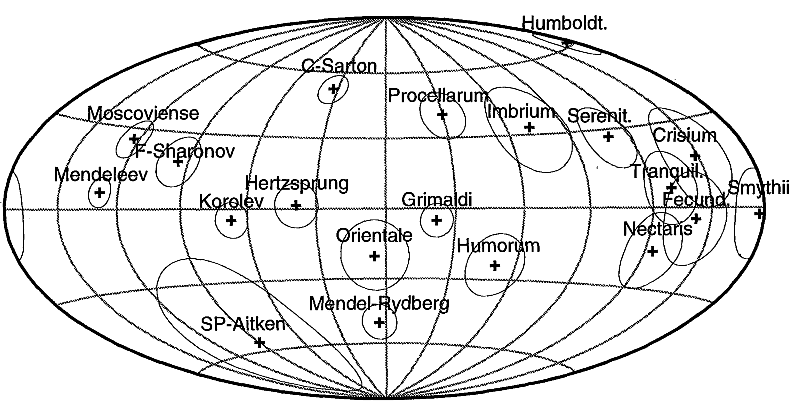

Fig. 1. Locations of major lunar basins. Here and in Fig. 2, longitude = 270° and the western limb of the moon as viewed from Earth is at the center front. The lunar near side is right of center and the lunar far side is left of center.

M. T. Zuber, Department of Earth and Planetary Sciences, Johns Hopkins University, Baltimore, MD 21218, USA, and Laboratory for Terrestrial Physics, NASA/Goddard Space Flight Center, Greenbelt, MD 20771, USA.
D. E. Smith, Laboratory for Terrestrial Physics, NASA/Goddard Space Flight Center, Greenbelt, MD 20771, USA.
F. G. Lemoine, Laboratory for Terrestrial Physics, NASA/Goddard Space Flight Center, Greenbelt, MD 20771, USA, and Astronomy Department, University of Maryland, College Park, MD 20742, USA.
G. A. Neumann, Department of Earth and Planetary Sciences, Johns Hopkins University, Baltimore, MD 21218, USA.

*To whom correspondence should be addressed.

details of the structure are obscured because it is largely covered by Orientale ejecta. There is also a circular depression ~700 km in diameter in the northwest Oceanus Procellarum (300°E, 40°N), to the southwest of another recently proposed impact structure (*12*). However, the topographic map does not show obvious evidence for a previously proposed massive (3200 km in diameter) nearside Oceanus Procellarum basin (*11*).

The gravitational signature of the moon was determined from velocity perturbations of the Clementine spacecraft as measured from the Doppler shift of the S-band radio tracking signal. Clementine was tracked by NASA's Deep Space Network (DSN) at Goldstone, California, Canberra, Australia, and Madrid, Spain, as well as by the Pomonkey, Maryland, tracking station operated by the Naval Research Laboratory. Data from the DSN sites typically had an accuracy of ~0.3 mm s^{-1} at 10-s intervals, whereas data from the Pomonkey site was accurate to ~3 mm s^{-1}. The tracking data were used to determine the Clementine orbit about the moon, as well as the lunar gravity field.

Clementine provided over 361,000 observations, of which ~57,000 were at spacecraft altitudes of less than 1000 km, and these data now constitute the strongest constraint on the long-wavelength gravity field of the moon. We combined the Clementine data with nearly 294,000 historical S-band tracking observations from Lunar Orbiters 2, 3, 4, and 5 and from the Apollo 15 subsatellite (*13*). These spacecraft lacked the global coverage of Clementine, but most had lower periapsis latitudes and thus provided distributed regions of short-wavelength resolution in the vicinity of spacecraft periapses (generally ±40° latitude).

In developing the gravity model, we applied an a priori power law constraint of the form $15 \times 10^{-5}/l^2$, where l is the spherical harmonic degree (*14*). This constraint has the effect of bounding the gravitational power in the wavelengths whose effect on the signal is at or below the noise level. In addition, we judiciously downweighted some of the low-altitude data to avoid artificial "striping" along orbit tracks in the field at short wavelengths. These techniques, which we have previously applied in models of the gravity fields of Earth, Mars, and Venus (*15*), have the advantage of preserving short-wavelength information in the field, where it is well resolved by the tracking data. Free-air gravity anomalies from our 70th-degree and -order spherical harmonic gravitational field model, designated Goddard Lunar Gravity Model 1 (GLGM-1), are shown in Fig. 2B.

Because of the moon's synchronous rotation, spacecraft cannot be directly tracked from Earth over a large part of the lunar far side, so there is no tracking data from 120° to 240° longitude in the ±45° latitude band. Nonetheless, orbiting spacecraft are sensitive to the positions of gravity anomalies even in areas without direct tracking, as evidenced by numerous anomalies in this region that correlate with major impact basins. However, the magnitudes of gravity anomalies in occulted regions are character-

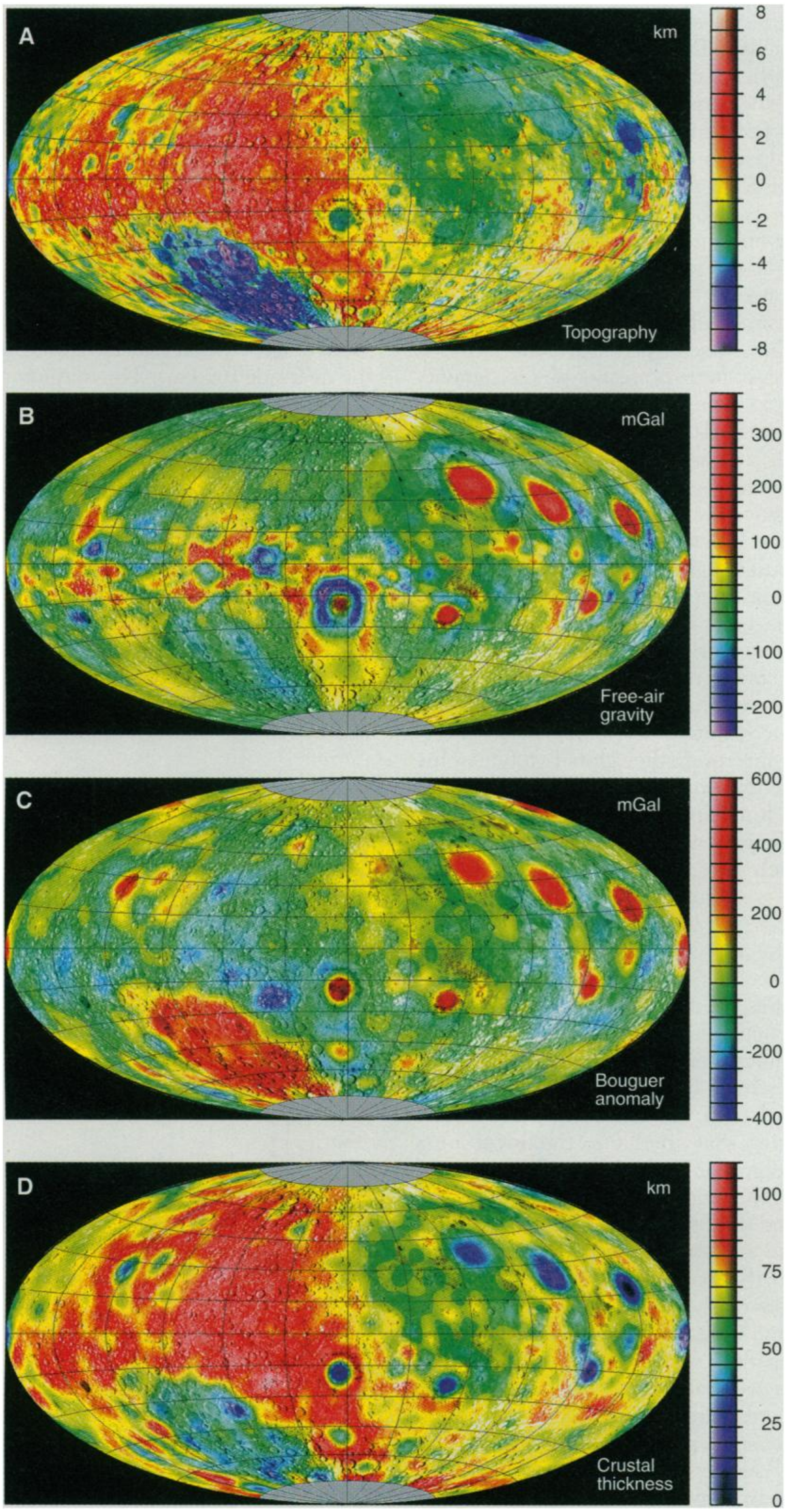

Fig. 2. **(A)** GLTM-1. **(B)** Free-air gravity anomalies from GLGM-1. **(C)** Bouguer gravity anomalies derived from global topography and free-air gravity models. **(D)** Uncorrected crustal thickness map based on a uniform-density crust and mantle. Other assumptions are discussed in the text.

ized by large errors. Gravity anomaly errors from GLGM-1 ranged from 22 milli-Galileos (mGal) (0.22 mm s^{-2} over the well-tracked near side at low latitudes to 47 mGal for the high-latitude far side.

We evaluated the global gravitational field of the moon at the surface, rather than at spacecraft altitude as done by others (*13, 16, 17*). In comparison with the most recent pre-Clementine gravity model of Konopliv and colleagues (*13*), GLGM-1 shows an ~10% greater range of anomalies when evaluated at an altitude of 100 km and, in addition, resolves some high-latitude farside structures not present in that model.

Figure 2B shows in red the gravity highs or "mascons" that correlate with the major nearside basins. The mascons, which were first recognized from Lunar Orbiter tracking data (*18*), are believed to be a consequence of the gravitational attraction of lava fill in mare basins (*19*) and of uplifted mantle beneath the basins (*20*). The improved short-wavelength control in our representation of the field, however, reveals that many of the mascons are ringed by negative anomalies outside the basins that suggest flexure of the lunar lithosphere in response to loading by the fill of mare lavas and uplifted mantle due to the impact process (*21*). Our model also shows gravitational signatures of several farside basins that have not previously been resolved or well resolved, including Hertzprung (232°E, 1°N), Korolev (203°E, 4°S), Mendeleev (141°E, 6°N), Freundlich-Sharonov (175°E, 18°N), and Moscoviense (147°E, 26°N).

Figure 2B shows that, as in previous lunar gravity models, the highland terrains are gravitationally smooth, indicating a state of isostatic compensation. For surface topography that is isostatically compensated, pressures caused by the weight of overlying rock balance at some depth beneath the surface. Isostatic equilibrium represents the state into which planetary topography tends to evolve with time and is indicated by a near-zero free-air gravity anomaly. In contrast to the highlands, lunar basins display a broad range of compensation states. Nearside mascon basins, which display large free-air positive anomalies, are distinctly uncompensated. Their gravitational signature indicates that surface topography is supported flexurally and demonstrates that in the vicinity of these impact structures, the lunar lithosphere (that is, the rigid outer shell) has displayed considerable strength since the time of loading (*22*). In contrast, the South Pole–Aitken Basin on the lunar far side has a modest free-air anomaly for its depth and is approximately 90% compensated. The 5-km-deep Mendel-Rydberg Basin shows a very small 25-mGal free-air anomaly and is almost fully compensated. Compensation states do not correlate simply with basin size or age. The range of compensation states of lunar basins indicates that the strength of the lunar lithosphere was likely to have been characterized by marked spatial variability at the time when the major basins formed and were subsequently flooded with mare basalts, and implies a complex lunar thermal history. Variations in the population of impactors (size, incidence angle, and velocity) could also contribute to the variable compensation states.

Figure 2B shows a marked asymmetry in the free-air gravitational signature of Mare Orientale, the youngest major impact basin on the moon (age, ~3.8 billion years) (*11*). This basin exhibits a comparatively modest 125-mGal mascon at basin center that is surrounded by a horseshoe-shaped gravity low with a maximum amplitude of −225 mGal centered on the inner and outer Rook rings. In contrast to the nearside basins that are encircled by negative anomalies outside the basins, the discontinuous negative is inside the Orientale Basin, and the basin is bounded by a gravity high centered on the Cordillera ring. Earlier studies have recognized a "bull's-eye" appearance of Orientale's gravity signature (*13, 17, 23*), but careful consideration of low-altitude orbital passes shows that the asymmetry is a characteristic feature of the basin.

To interpret the global topographic and gravitational observations in the context of lunar internal structure, we calculated Bouguer gravity anomalies (Fig. 2C), in which the gravitational attraction of surface topography (assuming a crustal density ρ_c = 2800 kg m^{-3}) is subtracted from the free-air anomaly to reveal the subsurface density distribution. Bouguer anomalies for the moon have previously been calculated both globally (*8*) and for major mare basins (*17, 24*), but detailed analyses have been limited because of errors of 12 to 70 mGal in the Bouguer correction that are due to the uncertainty of topographic knowledge. The relative errors in Clementine topography are governed by the orbit-to-orbit repeatability, of order 10 m, which translates to a 5-mGal error in the Bouguer anomaly, and by the precision of the altimeter system in both range and time, which is of order 10 mGal. In comparison with the errors in the gravity field discussed above, it is clear that Bouguer gravity errors are dominated by gravity error, in contrast to pre-Clementine analyses, in which Bouguer gravity error was dominated by errors in topography.

The simplest plausible interpretation of the Bouguer map is that subsurface mass differences are solely a consequence of crustal thickness variations. This interpretation is an oversimplification, but it provides a useful first-order indication of the variability of lunar internal structure. We have calculated uncorrected crustal thicknesses from the Bouguer gravity, assuming a reference value of 64 km in order to match the thickness of 56 km at the Apollo 12 and 14 sites (*25*). Figure 2D shows a degree 70 (80-km half-wavelength) resolution effective crustal thickness map in which we assume a constant-density crust and mantle (ρ_m = 3300 kg m^{-3}). For our assumed reference value, the crust composes 11% of lunar volume. The attraction of mare fill produces an error in crustal thickness of order 20% in flooded basins, and we have neglected this correction in making the global map.

Figure 2C shows that the farside crust is, on average, thicker (68 km) than that on the near side (60 km). The minimum crustal thickness is near zero beneath the Mare Crisium, with other notable areas of thin crust including the Orientale (4 km), Smythii (15 km), and South Pole–Aitken (20 km) basins. All resolvable lunar basins exhibit varying degrees of crustal thinning, which is likely the consequence of excavation and mantle rebound associated with the impact process (*17, 26*). The thickest crust (107 km) is on the far side in the vicinity of the Korolev Basin (also the region of highest topography), though on the

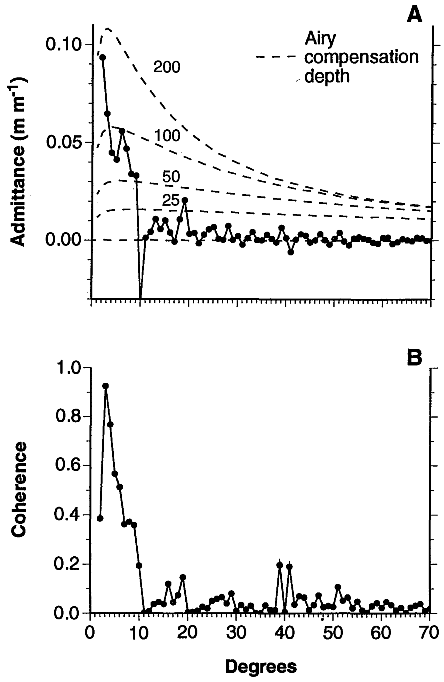

Fig. 3. (**A**) Admittance and (**B**) coherence spectra between gravity and topography. Calculations assume hydrostatic flattening. Shown in (A) as dashed lines are model admittances if Airy compensation is assumed, at depths shown in kilometers.

nearside southern hemisphere (30°S, 30°E) the crustal thickness reaches 95 km. The region of thick crust on the far side contributes substantially to the moon's center of mass–center of figure offset (9, 27), which we have recomputed from the spherical harmonic power spectra of gravity and topography and find to be 1.68 km ± 50 m in the Earth-moon direction, with the center of mass closer to Earth.

If the average farside crustal thickness is assumed, the area of anomalously thick crust on the far side has a volume comparable to that of the adjacent South Pole–Aitken Basin. This observation raises the intriguing question of whether the major topographic variation on the lunar far side is a consequence solely of enhanced melting related to the lunar magma ocean (to form the highland) or alternatively due to a combination of this process and impact ejecta from the South Pole–Aitken Basin or other basins or both.

Finally, in Fig. 3, we examine the global spectral properties of the moon by calculating admittance and coherence, which are power-spectral ratios of geoid (gravitational potential) and topography (28) that contain information about isostatic compensation mechanisms as a function of spatial wavelength. The degree 2 spherical harmonic terms show unusually low coherence related to long-wavelength complexities associated with the lunar flattening and the South Pole–Aitken Basin. Between spatial scales of 2000 km and 600 km (degrees 3 to 9) there is significant coherence and decreasing admittance. Features in this range include the lunar highlands and the largest impact basins. The negative admittance at degree 10 likely occurs because this wavelength is dominated by mare basins that are characterized by geoid highs and topographic lows. For features of spatial scale 500 km and smaller (degrees greater than 10), the geoid and topography are uncorrelated. In this wavelength range, most surface topography is supported by the strength of the lunar lithosphere, and the processes that produced topography and geoid anomalies do not result in simple global correlations of these quantities.

Figure 3A also shows the predicted admittance for a model with a linear isostatic response (28), with the assumption of compensation by an Airy mechanism at depths of 25, 50, and 100 km. In an Airy mechanism, topography is supported at a given depth by constant density columns of varying thickness (such as crustal thickness variations). The poor fit of the observed admittance to the model indicates that, unlike the case with other terrestrial planets (29, 30), there is no single Airy compensation depth that characterizes any wavelength range on the moon. Even at the longest wavelengths, which are typically Airy-compensated, lunar topography appears to be supported by multiple compensation mechanisms. For example, highland crust produced by the lunar magma ocean may be supported by density variations deep in the mantle, whereas some large basins may be compensated by shallower crustal thickness variations, and other basins may be uncompensated and supported by the strength of the moon's rigid outer shell. The global spectral character of the moon is therefore consistent with the full range of basin compensation states discussed above.

Several pre-Clementine studies have argued for a relatively "quiet" lunar stress state on the basis of the observed range of topography (31) and the power in the gravitational potential (29) as compared with Earth. These studies assumed that stresses arise solely from surface topography and that the gravity field is a consequence of topography that is Airy-compensated, even at wavelengths corresponding to major basins. However, we have shown that many of these basins are clearly uncompensated. Further, Clementine data have revealed more power in the lunar topographic and gravitational fields at long wavelengths and, in addition, show that large subsurface density variations contribute substantially to the gravity field over a range of wavelengths. These results indicate that the lunar lithosphere supports relatively large elastic stresses. Simple scaling relations of the power in the terrestrial and lunar gravity fields would suggest that the lunar stress state is much greater than previously thought, though long-wavelength stresses on Earth are mostly a consequence of mantle dynamics rather than of subsurface density variations as on the moon.

Topography and gravity from Clementine thus reveal a richer complexity in lunar structure and thermal history than had been previously appreciated. Detailed analysis of the global shape and modeling of individual features will provide further clarification of the nature of lunar evolution.

REFERENCES AND NOTES

1. S. R. Taylor, *Planetary Science: A Lunar Perspective* (Lunar and Planetary Institute, Houston, TX, 1982).
2. W. M. Kaula, *Icarus* **26**, 1 (1975); J. W. Head and S. C. Solomon, *Science* **213**, 62 (1981).
3. S. Nozette *et al.*, *Science* **266**, 1835 (1994).
4. B. H. Putney, The National Geodetic Satellite Program, General Theory for Dynamic Satellite Geodesy (1977); J. J. McCarthy *et al.*, NASA/Goddard Space Flight Center and Hughes/STX contractor report, GEODYN systems descriptions and operations manuals (1994). The GEODYN programs numerically integrate the spacecraft cartesian state and force-model partial derivatives by use of a high-order predictor-corrector model. The force model includes a spherical harmonic representation of the lunar and terrestrial gravity fields; point mass representations for the sun and other planets; lunar tides; and relativistic effects. Solar radiation pressure, tracking station measurement biases, and the elements of the orbit state are estimated for each data arc.
5. P. A. Regeon, R. J. Chapman, R. Baugh, *Int. Acad. Astron.* **IAA-L-0501**, 1 (1994).
6. The LIDAR contained a multistop detector that recorded the first trigger before and after the range window and up to four triggers inside the window, thus accepting up to four false triggers per shot due to either electronic instrument noise or background radiation at the laser wavelength.
7. A. Tarantola and B. Valette, *Rev. Geophys. Space Phys.* **20**, 219 (1982); J. A. Goff and T. H. Jordan, *J. Geophys. Res.* **93**, 13589 (1988).
8. B. G. Bills and A. J. Ferrari, *Icarus* **31**, 244 (1977).
9. W. M. Kaula, G. Schubert, R. E. Lingenfelter, W. L. Sjogren, W. R. Wollenhaupt, *Proc. Lunar Sci. Conf.* **3**, 2189 (1972); *ibid.* **4**, 2811 (1973); *Proc. Lunar Planet. Sci. Conf.* **5**, 3049 (1974).
10. D. E. Stuart-Alexander, *U.S. Geol. Surv. Map I-1047* (1992).
11. D. E. Wilhelms, *U.S. Geol. Surv. Prof. Pap. 1348* (1987).
12. A. McEwen, P. Davis, M. Howington-Kraus, M. Davies, *Lunar Planet. Sci. Conf.* **XXV**, (1994).
13. A. S. Konopliv, W. L. Sjogren, R. N. Wimberly, R. A. Cook, V. Alwar, "A high resolution lunar gravity field and predicted orbit behavior," AIAA Astrodynamics Specialist Conference, Victoria, B.C., Canada, 1993, pp. 93–622.
14. W. M. Kaula, *Theory of Satellite Geodesy* (Blaisdell, Waltham, MA, 1966).
15. J. G. Marsh, *et al.*, *J. Geophys. Res.* **95**, 22043 (1990); D. E. Smith *et al.*, *ibid.* **98**, 20871 (1993); R. S. Nerem, J. McNamee, B. G. Bills, *Geophys. Res. Lett.* **20**, 599 (1993).
16. W. L. Sjogren, J. Lorell, L. Wong, W. Downs, *J. Geophys. Res.* **80**, 2899 (1975).
17. S. R. Bratt, S. C. Solomon, J. W. Head, C. H. Thurber, *ibid.* **90**, 3049 (1985).
18. P. M. Muller and W. L. Sjogren, *Science* **161**, 680 (1968).
19. R. J. Phillips, J. E. Conel, E. A. Abbot, W. L. Sjogren, J. B. Morton, *J. Geophys. Res.* **77**, 7106 (1972).
20. W. M. Kaula, *Phys. Earth Planet. Int.* **2**, 123 (1969); D. U. Wise and M. Y. Yates, *J. Geophys. Res.* **75**, 261 (1970).
21. A simple calculation for a line load on a linear elastic plate, matching the radial positions of the maximum low and the transition from positive to negative anomalies, yields an elastic thickness for Mare Imbrium of 35 km.
22. S. C. Solomon and J. W. Head, *J. Geophys. Res.* **84**, 1667 (1979); *Rev. Geophys.* **18**, 107 (1980).
23. W. L. Sjogren and J. C. Smith, *Proc. Lunar Sci. Conf.* **3**, 2639 (1976).
24. R. J. Phillips and J. Dvorak, *Proc. Lunar Planet. Sci. Conf.* **12**, 91 (1981).
25. Y. Nakamura *et al.*, *ibid.* **10**, 2299 (1979); N. R. Goins, A. M. Dainty, M. N. Toksoz, *J. Geophys. Res.* **86**, 5061 (1981).
26. H. J. Melosh, *Impact Cratering: A Geologic Process* (Oxford Univ. Press, New York, 1989).
27. W. L. Sjogren and W. R. Wollenhaupt, *Moon* **15**, 143 (1976).
28. B. G. Bills and M. Kobrick, *J. Geophys. Res.* **90**, 827 (1985).
29. R. J. Phillips and K. Lambeck, *Rev. Geophys.* **18**, 27 (1980).
30. A. B. Kucinskas and D. L. Turcotte, *Icarus*, in press.
31. W. M. Kaula, M. J. Drake, J. W. Head, in *Satellites*, J. A. Burns and M. S. Matthews, Eds. (Univ. of Arizona Press, Tucson, 1986), pp. 581–629.

32. We are grateful to P. Rustan and the Clementine spacecraft, mission operations, and instrument engineers for outstanding support during the lunar mapping mission. We also thank I. Lewis and R. Reisse for assistance in understanding the lidar ranging data, D. Rowlands for modifying the GEODYN software for lunar orbiting spacecraft, A. Konopliv and W. Sjogren for providing the raw Lunar Orbiter tracking data, and A. Brenner, G. Elman, S. Fricke, and N. Pavlis for assistance in processing the tracking and altimetry data. We also thank B. Bills for helpful discussions and W. Kaula and S. Solomon for constructive reviews. The software used in this study was developed in support of the NASA Mars Observer and Mars Global Surveyor projects.

25 July 1994; accepted 1 November 1994